Journal of Medicinal Chemistry

Drug Annotation

Cite This: J. Med. Chem. 2020, 63, 52−65

pubs.acs.org/jmc

Discovery of a Covalent Inhibitor of KRAS^{G12C} (AMG 510) for the Treatment of Solid Tumors

Brian A. Lanman,*[,†] Jennifer R. Allen,[†] John G. Allen,[†] Albert K. Amegadzie,[†] Kate S. Ashton,[†] Shon K. Booker,[†] Jian Jeffrey Chen,[†] Ning Chen,[†] Michael J. Frohn,[†] Guy Goodman,[†] David J. Kopecky,[†] Longbin Liu,[†] Patricia Lopez,[†] Jonathan D. Low,[†] Vu Ma,[†] Ana E. Minatti,[†] Thomas T. Nguyen,[†] Nobuko Nishimura,[†] Alexander J. Pickrell,[†] Anthony B. Reed,[†] Youngsook Shin,[†] Aaron C. Siegmund,[†] Nuria A. Tamayo,[†] Christopher M. Tegley,[†] Mary C. Walton,[†] Hui-Ling Wang,[†] Ryan P. Wurz,[†] May Xue,[†] Kevin C. Yang,[†] Pragathi Achanta,[‡] Michael D. Bartberger,[§] Jude Canon,[‡] L. Steven Hollis,[#] John D. McCarter,[∥] Christopher Mohr,[§] Karen Rex,[‡] Anne Y. Saiki,[‡] Tisha San Miguel,[∥] Laurie P. Volak,[⊥] Kevin H. Wang,[▽] Douglas A. Whittington,[▽] Stephan G. Zech,[#] J. Russell Lipford,[‡] and Victor J. Cee[†]

Departments of [†]Medicinal Chemistry, [‡]Oncology Research, [§]Molecular Engineering, [∥]Discovery Technologies, and [⊥]Pharmacokinetics and Drug Metabolism, Amgen Research, One Amgen Center Drive, Thousand Oaks, California 91320, United States

Departments of [#]Discovery Attribute Sciences and [▽]Molecular Engineering, Amgen Research, 360 Binney Street, Cambridge, Massachusetts 02142, United States

Supporting Information

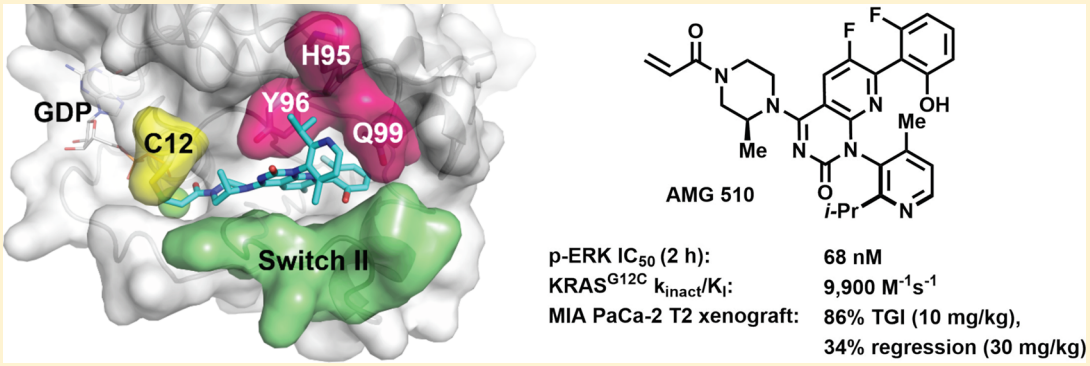

ABSTRACT: KRAS^{G12C} has emerged as a promising target in the treatment of solid tumors. Covalent inhibitors targeting the mutant cysteine-12 residue have been shown to disrupt signaling by this long-"undruggable" target; however clinically viable inhibitors have yet to be identified. Here, we report efforts to exploit a cryptic pocket (H95/Y96/Q99) we identified in KRAS^{G12C} to identify inhibitors suitable for clinical development. Structure-based design efforts leading to the identification of a novel quinazolinone scaffold are described, along with optimization efforts that overcame a configurational stability issue arising from restricted rotation about an axially chiral biaryl bond. Biopharmaceutical optimization of the resulting leads culminated in the identification of AMG 510, a highly potent, selective, and well-tolerated KRAS^{G12C} inhibitor currently in phase I clinical trials (NCT03600883).

INTRODUCTION

Mutations in the *RAS* oncogene are the most common activating mutation in human cancer, occurring in 30% of human tumors.[1] Although the *RAS* gene family comprises three isoforms (*KRAS*, *HRAS*, and *NRAS*), 85% of *RAS*-driven cancers are caused by mutations in the *KRAS* isoform,[2] with mutations occurring most frequently in solid tumors such as lung adenocarcinoma, pancreatic ductal carcinoma, and colorectal carcinoma.[1] Among *KRAS* mutant tumors, 80% of all oncogenic mutations occur within codon 12, with the most common mutations being *p.G12D* (41%), *p.G12V* (28%), and *p.G12C* (14%).[3]

In growth factor signaling pathways, the KRAS protein functions as a molecular switch, regulating proliferation by alternating between a guanosine diphosphate (GDP)-bound inactive form and a guanosine triphosphate (GTP)-bound active form capable of engaging downstream effector proteins

Received: July 21, 2019
Published: December 10, 2019

DOI: 10.1021/acs.jmedchem.9b01180
J. Med. Chem. 2020, 63, 52−65

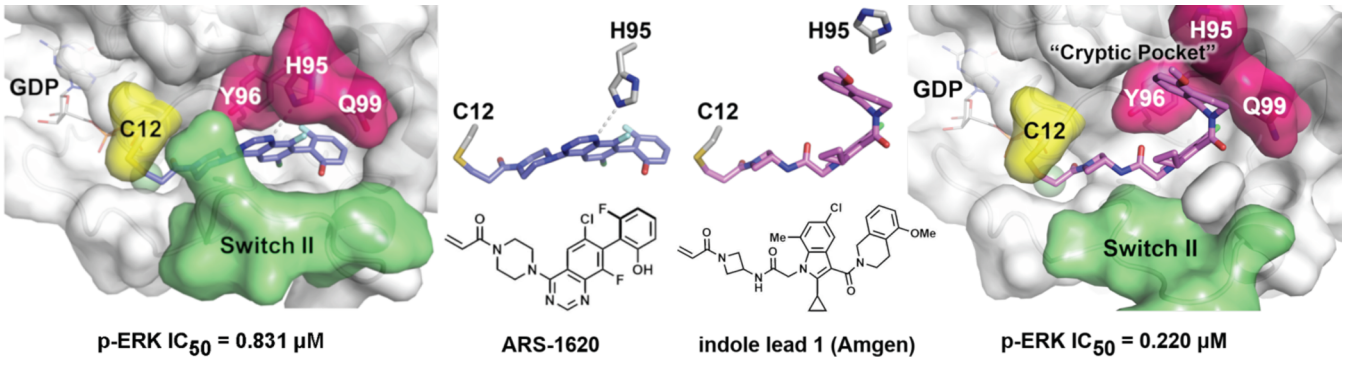

Figure 1. Comparison of the GDP-KRAS^{G12C} binding modes of ARS-1620 (blue, PDB code 5V9U)[6] and the internally identified indole lead **1** (pink, PDB code 6P8Z).[7] The tetrahydroisoquinoline portion of indole **1** engages a "cryptic pocket" (magenta) not exploited by prior inhibitors, which is induced by side chain rotation of H95 and comprises the residues Y96, H95, and Q99. Inhibitor activity on downstream ERK phosphorylation (p-ERK IC_{50}, 2 h incubation) is indicated.

to elicit a pro-proliferative response. Codon 12 mutations impair the regulated cycling between these two forms by disrupting the association of GTPase-activating proteins (GAPs), impairing the inactivation of KRAS and leading to the accumulation of the pro-proliferative form.

Despite being one of the first oncogenes identified, 3 decades of effort have failed to identify clinically useful inhibitors of the KRAS protein.[4] Two features of KRAS confound its tractability as a drug target: (1) KRAS binds to GDP and GTP with picomolar affinity, severely hindering efforts to develop nucleotide-competitive inhibitors, and (2) the KRAS protein lacks other deep surface hydrophobic pockets, thwarting efforts to identify high-affinity allosteric inhibitors.[1]

In 2013, Shokat and co-workers reported a novel strategy aimed at overcoming these challenges that used a covalent inhibitor to target the reactive cysteine-12 of KRAS^{G12C}.[5] They envisioned that covalent modification of Cys12 would allow for persistent disruption of KRAS^{G12C}-driven pro-proliferative signaling by allowing relatively low-affinity, noncovalent interactions to selectively template the formation of a covalent bond between the inhibitor and KRAS, resulting in the permanent inactivation of the adducted protein. In addition to providing a means of overcoming the poor "druggability" of KRAS, it was hoped that this strategy might also allow for the selective growth inhibition of *KRAS* mutant cells (i.e., tumors) while sparing nonmutant cells (i.e., normal tissue), potentially overcoming the anticipated toxicological challenges posed by nonselective inhibition of *KRAS*-driven cell growth.

After significant optimization efforts, early hits identified by the Shokat group were modified to provide a tool compound suitable for in vivo applications, ARS-1620 (Figure 1).[8,9] A cocrystal structure of ARS-1620 with KRAS^{G12C} confirmed that ARS-1620 covalently bound to cysteine-12 of the GDP-bound form of KRAS, with the quinazoline core of the molecule occupying an allosteric pocket (the "switch II pocket" (S-IIP)) located beneath the effector protein-engaging switch II loop region of the protein. While this adduct demonstrated promising antiproliferative activity against *KRAS p.G12C* mutant tumors both in vitro and in vivo,[9] further improvements in cellular potency appeared necessary to deliver a therapeutically useful molecule. Here, we describe efforts at Amgen to discover and develop a targeted covalent inhibitor of KRAS^{G12C} suitable for clinical application.

RESULTS AND DISCUSSION

Prior to the Shokat lab's initial disclosure of their efforts targeting KRAS^{G12C}, we had independently initiated our own research program to identify covalent inhibitors of KRAS^{G12C}, driven by the same strategic considerations. To support our initial screening efforts and provide access to focused libraries of cysteine-reactive compounds, we entered into a collaboration with Carmot Therapeutics. Using Carmot's Chemotype Evolution platform,[10] we identified a series of selective covalent inhibitors of KRAS^{G12C} that were optimized (via structure-based design and additional rounds of targeted library synthesis) to provide advanced lead **1**, which potently inactivated KRAS^{G12C} in biochemical and cellular assays.[7]

Cocrystallization of **1** with GDP-KRAS^{G12C} revealed compound **1** to adopt a novel binding mode relative to ARS-1620, with the tetrahydroisoquinoline ring of **1** occupying a previously unexploited cryptic pocket on the surface of KRAS unveiled by rotation of the histidine-95 side chain and comprising portions of H95, Y96, and Q99 (Figure 1).[11] Although engagement of this cryptic pocket led to a multifold enhancement in cellular potency relative to ARS-1620, compound **1** suffered from very high clearance and low oral bioavailability in rodent model systems, making it unsuitable for in vivo use. We therefore sought alternative means of exploiting the H95/Y96/Q99 cryptic pocket that might deliver leads with improved pharmaceutical properties.

Superposition of the binding modes of indole lead **1** and ARS-1620 (Figure 2) suggested that substitution of the quinazoline nitrogen (N1) of ARS-1620 might provide an alternative means of accessing the H95 cryptic pocket and thus of generating new, enhanced-potency inhibitors of KRAS^{G12C}.

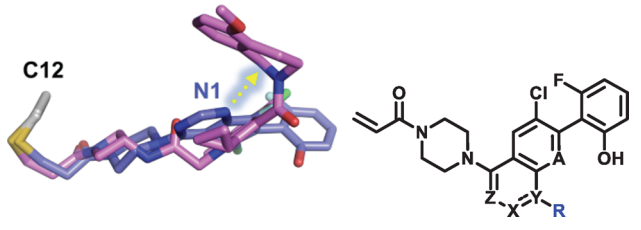

Figure 2. Overlay of the GDP-KRAS^{G12C}-bound conformations of ARS-1620 (blue) and indole lead **1** (pink), suggesting potential access to the Y96/H95/Q99 cryptic pocket by substitution of the N1 position of the ARS-1620 scaffold. Conceptual hybrid structure is shown at right.

DOI: 10.1021/acs.jmedchem.9b01180
J. Med. Chem. 2020, 63, 52−65

Such a strategy was expected to face some challenges: our prior efforts to modify the quinazoline core of ARS-1620 had shown that perturbation of the hydrogen bond between N1 and the H95 side chain of KRAS typically led to significant losses in functional activity. Nevertheless, as this strategy promised to identify new alternatives to the metabolically labile **1**, we pursued this approach, anticipating that a successful hybrid molecule would not only deliver enhanced potency (via effective engagement of the cryptic pocket)[12] but also improved ADME properties.

To test this hypothesis, we prepared a series of phthalazine analogues, wherein the C4 position (Y) of the phthalazine core (X = N, Y = C) was substituted with a range of aryl substituents (Table 1). We used a pair of assays to gauge the ability of the resulting analogues to disrupt KRAS-mediated signaling: (1) a cell-free AlphaScreen assay,[13] which measured inhibition of SOS1-catalyzed GDP/GTP exchange by monitoring the disruption of the interaction between GTP-KRAS^{G12C} and the Ras binding domain (RBD) of c-RAF, and (2) a cell-based phospho-ERK1/2 immunoassay (MSD),[14] which detected decreased ERK phosphorylation resulting from disrupted upstream KRAS signaling. Phenyl substitution of C4 (**2**) led to an analogue ~20-fold less potent than ARS-1620 in our exchange assay (IC_{50} = 20.1 μM) and 70-fold less potent in our p-ERK cellular assay (IC_{50} = 58 μM).

Table 1. Biochemical and Cellular Activity of Hybrid Scaffolds Designed To Access the Y96/H95/Q99 Cryptic Pocket

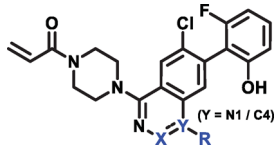

Cmpd	X	Y	R	Exchange IC_{50} (μM)[a]	p-ERK IC_{50} (μM)[b]
ARS-1620	CH	N	--	0.939	0.831
2	N	C		20.1	58.0
3	N	C	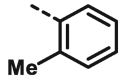	5.71	3.33
4	N	C	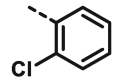	3.52	3.53
5	N	C	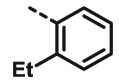	0.903	2.58
6	N	C	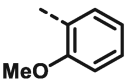	9.15	8.05
7	N	C	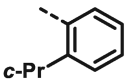	1.55	7.15
8	N	C	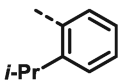	0.683	1.80
9	CO	N	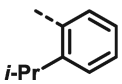	0.101	0.335

[a]SOS1-catalyzed GDP/GTP exchange (AlphaScreen, KRAS^{G12C}/c-RAF Ras binding domain), 5 min incubation.[15] [b]p-ERK1/2 immunoassay (MSD), EGF-stimulated MIA PaCa-2 cells, 2 h incubation.[16] All data represent $n \geq 2$.

Cocrystallization of compound **2** with GDP-KRAS^{G12C} confirmed that compound **2** adopted a similar binding mode to ARS-1620 but with the newly introduced C4 phenyl substituent occupying the H95/Y96/Q99 cryptic pocket, as designed (Figure 3a). The C4 phenyl group, however, failed to make many noncovalent contacts with the cryptic pocket residues (e.g., Y96), prompting us to examine whether further substitution of the phenyl ring could produce additional contacts with the cryptic pocket residues that would lead to enhanced potency.

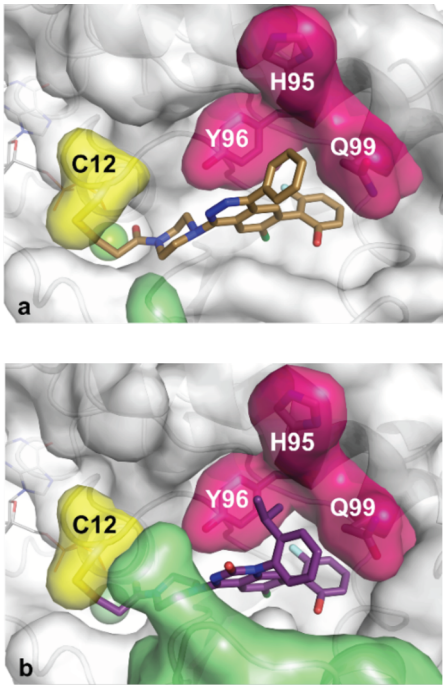

Figure 3. X-ray crystallography confirms hybrid scaffolds **2** (a; tan, PDB code 6PGO) and **9** (b; violet, PDB code 6PGP) access the cryptic pocket. Additional van der Waals contacts between the isopropyl moiety of **9** and H95, Y96, and Q99 account for the increased biochemical and cellular potency of **9**.

To test this hypothesis, a series of increasingly large ortho-substituents were added to the phenyl ring of **2** (see compounds **3**–**8**, Table 1) with the aim of enhancing contacts with Y96. Encouragingly, methyl substitution (**3**) provided a 4-fold increase in biochemical potency and 17-fold increase in cellular activity, and ethyl substitution (**5**) led to further gains in potency (exchange IC_{50} = 0.903 μM, p-ERK IC_{50} = 2.6 μM). Isopropyl substitution (**8**) proved optimal, however, demonstrating biochemical and cellular IC_{50} values on a par with ARS-1620.

In an effort to further enhance the potency of these initial leads, we also examined the effect of changing the phthalazine core of **8**. Notably, quinazolinone **9** (X = CO, Y = N; Table 1) was found to offer a significant improvement in biochemical and cellular potency relative to **8**, with the resulting compound

DOI: 10.1021/acs.jmedchem.9b01180
J. Med. Chem. 2020, 63, 52−65

Table 2. Optimization of the Piperazine Substituent (R^2) and Lipophilic "Tail" (R^1) Regions of (*R*)-9 Enhances Potency and Bioavailability

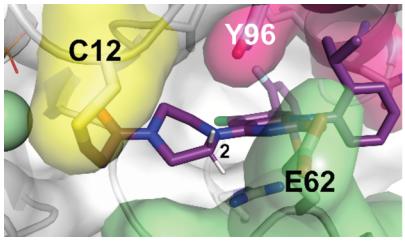

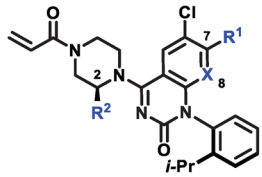

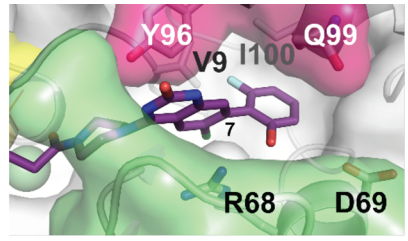

Cmpd	R^{1a}	R^2	X	p-ERK IC_{50} MIA PaCa-2 (μM)[b]	Viability IC_{50} MIA PaCa-2 | A549 (μM)[c]	Mu | H hep CL_{int} (μL/min/10^6 cells)	MDCK Permeability A–B (μcm/s)	HT Solubility (μM, PBS | FaSSIF | 0.01 N HCl)	Mouse CL (L/h/kg) | Vss (L/kg) | $t_{1/2}$ (h) | %F[d]
(*R*)-**9**		H	CH	0.130	0.033 | 10.3	195 | 56	2	0 | 191 | 0	0.3 | 0.8 | 3.4 | <0.5
10	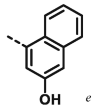	H	CH	--	0.017 | 2.7	|	--	0 | 71 | 0	| | |
(*R*)-**11**	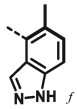	H	CH	0.008	0.004 | 1.7	180 | 121	4	0 | 218 | 0	4.2 | 5.3 | 2.8 | <0.5
(*R*)-**12**		H	CH	0.080	0.022 | 6.4	415 | 197	7	0 | 344 | 0	| | |
(*R*)-**13**		Me	CH	0.047	0.006 | 5.8	356 | 166	10	0 | 260 | 0	1.6 | 1.4 | 0.9 | 12
(*R*)-**14**		Me	CH	0.220	0.018 | 7.4	397 | 317	6	0 | 255 | 0	| | |
15		Me	CH	0.442	0.040 | 7.4	270 | 148	3	0 | 218 | 0	| | |
(*R*)-**16**		Me	CH	0.028	0.014 | 15.3	263 | 113	1	0 | 226 | 0	| | |
(*R*)-**17**		H	N	0.069	0.011 | 11.5	109 | 32	6	14 | 204 | 14	0.8 | 0.5 | 1.5 | 1.3
(*R*)-**18**		Me	N	0.044	0.005 | 14.2	119 | 38	9	9 | 184 | 7	0.4 | 0.4 | 1.3 | 33
(*R*)-**19**		Me	N	0.066	0.005 | 7.9	236 | 135	20	11 | 224 | 0	3.6 | 2.3 | 0.6 | 9
(*R*)-**20**		Me	N	0.056	0.016 | 7.1	319 | 205	12	0 | 175 | 0	5.4 | 4.8 | 0.6 | 12
(*R*)-**21**		Me	N	0.146	0.013 | 12.2	288 | 82	18	88 | 299 | 57	1.7 | 0.8 | 0.5 | 10

[a]Unless noted, separable C7 biaryl bond atropisomers were not observed. [b]p-ERK1/2 immunoassay (MSD), 2 h incubation. [c]Viability assessed at 72 h by CellTiter-Glo luminescence assay (Promega) in MIA PaCa-2 (*p.G12C*) and A549 (*p.G12S*) cell lines. All data represent $n \geq 2$. [d]iv/po dosing in BALB/c mice (vehicle: iv, 1 mg/kg, DMSO; po, 10 mg/kg, 1% Tween 80, 2% HPMC, 97% water). [e]Mixture of four atropisomers (isopropylphenyl and naphthol biaryl bonds). [f]Single indazole biaryl bond atropisomer. [g]Mixture of isopropylphenyl atropisomers.

proving ~3–9 times more potent than ARS-1620 in in vitro assays.[17]

Cocrystallization of compound **9** with GDP-$KRAS^{G12C}$ (Figure 3b) confirmed **9** to adopt a binding mode in which the isopropylphenyl substituent was positioned in close contact with the Y96, H95, and Q99 residues of the cryptic pocket and one in which the isopropylphenyl and phthalazine rings were nearly orthogonally oriented. Although compound **9** consisted of a mixture of atropisomers about the biaryl C–N bond (due to restricted rotation about the bis-ortho-substituted biaryl linkage), only the *R*-atropisomer[18] showed significant occupancy of the switch II pocket crystallographically.

DOI: 10.1021/acs.jmedchem.9b01180
J. Med. Chem. 2020, 63, 52–65

Separation of the *R*- and *S*-atropisomers by chiral chromatography confirmed (*R*)-**9** to be significantly more potent than the corresponding *S*-atropisomer.[19] Accordingly, subsequent studies were performed with the atropisomer which oriented its larger ortho substituent toward the Y96/H95/Q99 cryptic pocket (typically the *R*-atropisomer) (Table 2).

Although (*R*)-**9** proved to be an exceptionally potent inhibitor of $KRAS^{G12C}$ signaling (p-ERK IC_{50} = 0.130 μM), the GDP-$KRAS^{G12C}$ cocrystal structure suggested several prospects for further optimization: (1) substitution of the piperazine C2 position appeared to offer an opportunity to enhance activity through additional contacts with C12, E62, and Y96 and (2) replacement of the fluorophenol "tail" of (*R*)-**9** appeared to offer an opportunity to form more extensive contacts with lipophilic residues (e.g., V9 and I100) and to modulate polar interactions with R68 or D69. Additionally, despite the promising potency profile of (*R*)-**9**, PK studies revealed no measurable oral bioavailability in BALB/c mice. Low membrane permeability (2 μcm/s in a Madin–Darby canine kidney (MDCK) cell trans-well permeability assay) and relatively poor aqueous solubility (Table 2) were viewed as likely contributing factors. Therefore, C2 and C7 modifications were also viewed as potential opportunities to modulate the biopharmaceutical properties of (*R*)-**9** to enhance the bioavailability of future analogues.

We began our SAR efforts around (*R*)-**9** by replacing its C7 fluorophenol moiety with larger groups designed to make additional contacts with residues in the "tail" subpocket. While we continued to employ an ERK phosphorylation assay as our primary screen for KRAS-based cell activity, we also profiled new compounds in CellTiter-Glo-based proliferation assays[20] using *KRAS p.G12C* (MIA PaCa-2) and *KRAS p.G12S* (A549) cells to confirm that growth-inhibitory activity was specific to *p.G12C* mutant cells and sparing of those in which Gly12 was instead mutated to serine (G12S). Naphthol (**10**) and indazole (**11**) substituents did indeed show enhanced activity in ERK phosphorylation and viability assays (Table 2); however these analogues continued to demonstrate poor aqueous solubility, low MDCK permeability, and in the case of indazole **11**, no improvement in oral bioavailability.

In an effort to enhance MDCK permeability, we examined the effect of removing the phenolic moiety from (*R*)-**9** to provide fluorophenyl **12**. Interestingly, this modification led to no loss in activity in either the p-ERK or viability assays and a more than 3-fold increase in MDCK permeability. Good MDCK permeability was also retained in a related analogue wherein a piperazine C2-methyl substituent was introduced (**13**). Notably, methylpiperazine **13** demonstrated not only further improvements in cellular activity (p-ERK IC_{50} = 47 nM) but also measurable mouse oral bioavailability (12%). Attempts to replace the fluorophenyl tail of **13** with larger lipophilic substituents (e.g., *o*-chlorophenyl (**14**) or *o*-trifluorotolyl (**15**)) proved detrimental, however, and led to reduced cellular activity and MDCK permeability. Likewise, while reintroduction of the phenolic moiety into **13** (to provide fluorophenol **16**) again had minimal impact on cellular activity, membrane permeability was dramatically reduced (P_{AB} = 1 μcm/s).

With the phenolic functionality of (*R*)-**9** and (*R*)-**16** emerging as a key contributor to the reduced MDCK permeability of these analogues, we also decided to examine an alternative strategy to mitigate the adverse effect of this group. As desolvation of the phenol during membrane diffusion was hypothesized to add to the energetic cost of membrane permeation, we investigated whether nitrogen incorporation at the C8 position of the quinazolinone ring could enhance MDCK permeability by providing an internal hydrogen-bond acceptor to satisfy the adjacent phenolic donor during membrane permeation.[21] Gratifyingly, azaquinazolinones **17** and **18** both demonstrated not only significantly enhanced MDCK permeability relative to their nonaza congeners (**9** and **16**) but also significantly improved aqueous solubility. While the oral bioavailability of compound **17** remained disappointing (1.3%), azaquinazolinone **18** demonstrated significantly enhanced oral bioavailability (33%) and excellent cellular activity (p-ERK IC_{50} = 44 nM; MIA PaCa-2 viability IC_{50} = 5 nM).

While further improvements in MDCK permeability could be achieved by removing the phenolic functionality from compound **18** (see compounds **19** and **20**), the resulting compounds suffered from reduced bioavailability and increased in vivo clearance relative to **18**. Similarly, although removal of the fluorine substituent from **18** (to provide phenol **21**) enhanced both MDCK permeability and aqueous solubility, such benefits came at the cost of reduced potency, metabolic stability, and oral bioavailability. Thus, due to its unique balance of promising pharmacokinetic profile and excellent potency, azaquinazolinone **18** became our new lead for subsequent optimization.

Disappointingly, we soon discovered a new challenge with compound **18**, originating in the axial chirality of its isopropylphenyl–quinazolinone biaryl bond. Although the sterically congested environment about this bond dramatically restricted rotation, giving rise to separable atropisomers, it unfortunately did not *completely* restrict rotation about this bond. Slow interconversion of the *R*- and *S*-atropisomers occurred at 25 °C with a half-life of 8 days and an interconversion free energy barrier ($\Delta G^{\ddagger}$) of 26 kcal/mol,[22] behavior that promised to greatly complicate the development of (*R*)-**18** as a pure substance (Figure 4).

Strategies for addressing atropisomerism in drug discovery have previously been reviewed,[23] however, and drawing upon this guidance, we initiated a trio of strategies to identify a lead molecule with atropisomer configurational properties suitable for drug development needs. These strategies included (1)

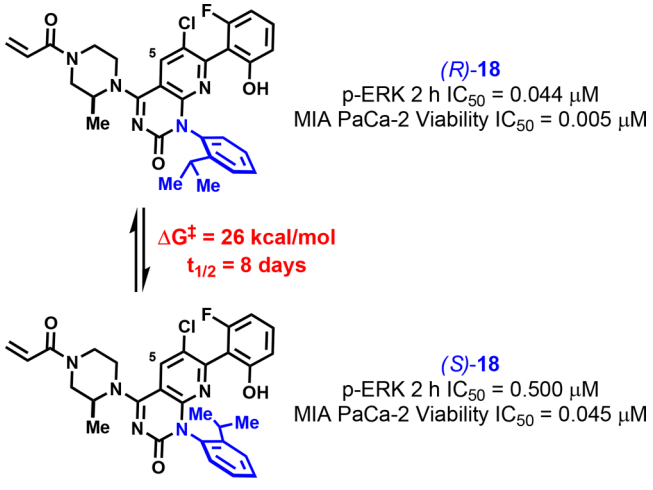

Figure 4. Compound **18** atropisomers are not configurationally stable at 25 °C.

DOI: 10.1021/acs.jmedchem.9b01180
J. Med. Chem. 2020, 63, 52–65

raising the energetic barrier to atropisomer interconversion ($\Delta G^{\ddagger}$ > 30 kcal/mol) to allow for the development of a single, pure atropisomer, (2) lowering the interconversion barrier ($\Delta G^{\ddagger}$ < 20 kcal/mol) to allow for the development of a freely interconverting mixture of atropisomers, or (3) symmetrizing the cryptic pocket substituent to avoid the generation of an axis of chirality.

We used two methods to assess the atropisomer interconversion free-energy barriers of our lead molecules: slowly interconverting atropisomers were assessed using time-course ^{1}H NMR experiments, fitting atropisomer ratio information with the Eyring equation to determine $\Delta G^{\ddagger}$; rapidly interconverting atropisomers, in contrast, were assessed using the VT NMR method described in Figure 5.[24]

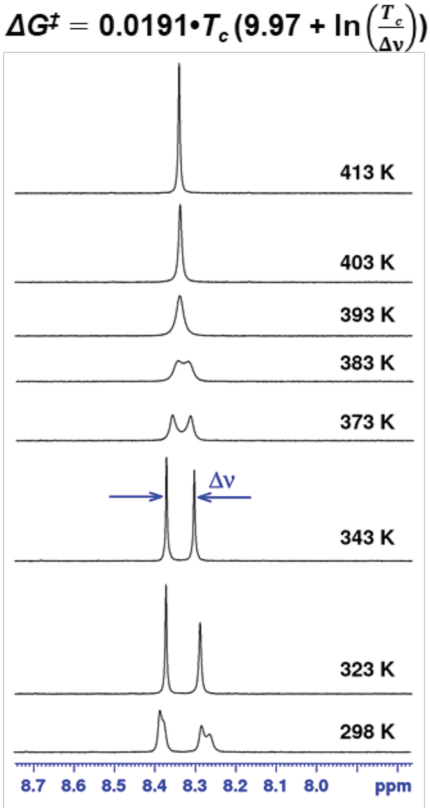

Figure 5. VT NMR method for determining atropisomer interconversion free energy barriers ($\Delta G^{\ddagger}$). Coalescence of the H5 ^{1}H NMR resonance was monitored at elevated temperature, and the coalescences temperature (T_c) and chemical shift difference ($\Delta\nu$; slow exchange limit) were used for calculation of $\Delta G^{\ddagger}$. (Compensation applied for minor temperature dependence in the H5 chemical shift.) ^{1}H spectra (DMSO-d_6) for compound **27** are depicted. At 298 K, methylpiperazine conformational exchange causes H5 line broadening, which is averaged out at T > 320 K.

We first explored methods to further restrict rotation about the isopropylphenyl−quinazolinone biaryl bond, probing the effect of *ortho*-substituent steric demand on the rotational free-energy barrier. While replacement of isopropyl substituent with a cyclopropyl ring (**22**) did little to alter the atropisomer interconversion barrier (and led to some loss in activity, see Table 3), introduction of a *tert*-butyl group (**23**) led to significantly increased configurational stability, with minimal loss in activity. Bis-ortho substitution (**24**) proved optimal, however, both locking of rotation about the biaryl bond ($\Delta G^{\ddagger}$

Table 3. Atropisomer Stability and KRAS^{G12C} Activity as a Function of Cryptic Pocket Arene Identity and Substitution Pattern

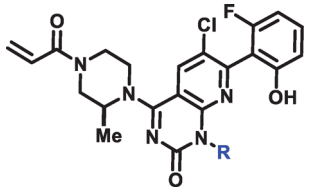

Cmpd	R[a]	Exchange IC_{50} (μM)[b]	p-ERK IC_{50} (μM)[c]	Interconversion barrier ($\Delta G^{\ddagger}$, kcal/mol)[d]
(*R*)-**18**	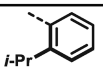	0.051	0.044	26.0[1]
22		0.225	0.109	25.0[1]
(*R*)-**23**		0.117	0.051	>30[2]
(*R*)-**24**		0.025	0.028	>30[2]
25		0.127	0.025	29.0[2]
26		0.083	0.053	23.5[2]
27		0.164	0.218	21.5[2]
28		0.081	0.063	17.5[2]
(*R*)-**29**		0.053	0.127	25.8[1]
30		0.306	0.199	NA
31		0.068	0.036	NA
32	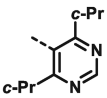	0.034	0.036	NA
33	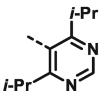	0.021	0.025	NA

[a]Atropisomer configuration assigned by cocrystallization with GDP-KRAS^{G12C} except for compound **29** (configuration assigned by analogy; more potent isomer assigned *R*-configuration). [b]SOS1-catalyzed GDP/GTP exchange (AlphaScreen, KRAS^{G12C}/c-RAF Ras binding domain), 5 min incubation. [c]p-ERK1/2 immunoassay (MSD), 2 h incubation. All data represent $n \geq 2$. For separable atropisomers, data are reported for the more potent *R*-atropisomer, as depicted. [d]Atropisomer interconversion barrier ($\Delta G^{\ddagger}$) as determined by [1]time-course NMR experiment or [2]VT NMR.

DOI: 10.1021/acs.jmedchem.9b01180
J. Med. Chem. 2020, 63, 52−65

> 30 kcal/mol) and leading to enhanced biochemical and cellular activity (p-ERK IC_{50} = 28 nM). The isopropyl group in **24** proved crucial to this effect, as its replacement with a nonbranched ethyl substituent (**25**) led to a significant reduction in the biaryl rotational barrier ($\Delta G^{\ddagger}$ = 29.0 kcal/mol), as well as some loss in biochemical potency.

We next examined whether replacement of the isopropylphenyl ring of (*R*)-**18** with less sterically demanding groups could lower the rotational barrier sufficiently to restore free rotation about the biaryl bond. Replacing the isopropylphenyl group with an analogous isopropylpyridine (cf., compound **26**) meaningfully reduced the rotational barrier ($\Delta G^{\ddagger}$ = 23.5 kcal/mol); however the resulting atropisomers remained metastable ($t_{1/2}$ ~ 5 h at 25 °C) and unsuitable for further development. Contraction of the pendant six-membered ring to a five-membered ring (cf., pyrazole **27**) further reduced the rotational barrier ($\Delta G^{\ddagger}$ = 21.5 kcal/mol) but failed to fully free rotation about the biaryl bond and led to moderate losses in biochemical and cellular potency. Introducing a sulfur atom at the open ortho-position of the five-membered ring (c.f., **28**), however, restored free rotation about the biaryl bond and restored biochemical and cellular activity. Interestingly, attempts to fully restrict biaryl bond rotation by bis-ortho-substitution of five-membered ring cryptic pocket substituents (cf., **29**) were unsuccessful, contrasting with this strategy's success in the context of six-membered rings substituents (cf., (*R*)-**24**). These studies hence reveal biaryl bond rotation to be influenced by a complex interplay of factors including substituent size, substitution pattern, and ring size.

As a final strategy to avoid configurationally unstable biaryl bond atropisomers, we examined the properties of symmetrically bis-ortho-substituted cryptic pocket substituents. Although bis-methyl substitution (**30**) failed to afford a potent lead, bis-ethyl (**31**), cyclopropyl (**32**), and isopropyl (**33**) substitution all afforded compounds with good biochemical and cellular activity and no potential to generate rotational atropisomers.

Although all three strategies to address the axial chirality/configurational stability issue were ultimately successful in identifying potent $KRAS^{G12C}$ inhibitors suitable for subsequent development, the resulting leads demonstrated quite distinct pharmacological profiles when dosed orally (10 mg/kg) in BALB/c mice (Table 4). Whereas (*R*)-**24** showed moderate oral bioavailability (21%) and good in vivo target coverage (4.5× coverage of the p-ERK IC_{50} at C_{max}),[25] compound **28** demonstrated much more modest in vivo target coverage, and compounds **31**−**33** failed to show appreciable in vivo target coverage, even at C_{max}, possibly due in part to the reduced oral bioavailability of these analogues. (*R*)-**24** thus became our lead candidate for subsequent pharmacodynamic and efficacy testing in xenograft models.

Table 4. Mouse PK Profiles[a] of Compounds with Atropisomer Configurational Properties Suitable for Development

cmpd	CL (L h^{-1} kg^{-1})	PPB (f_u)[b]	$t_{1/2}$ (h)	F (%)	10 mg/kg $C_{max,u}$[c]/ p-ERK IC_{50}
(*R*)-**24**	2.7	0.03	0.5	21	4.5
28	2.2	0.02	1.1	22	1.5
31	3.3	0.03	0.5	8	0.8
32	3.3	0.08	0.5	7	0.6
33	2.3	0.03	0.8	13	0.8

[a]iv/po dosing in BALB/c mice (vehicle: iv, 1 mg/kg, DMSO; po, 10 mg/kg, 1% Tween 80, 2% HPMC, 97% water). [b]PPB by ultracentrifugation. [c]Maximum unbound plasma concentration (C_{max}:f_u).

To test the effect of (*R*)-**24** on KRAS signaling in vivo, (*R*)-**24** was dosed orally in athymic nude mice that had been subcutaneously implanted with MIA PaCa-2 T2 human tumor cells (homozygous *KRAS p.G12C*). Serum and tumor samples were collected 2 h postdosing, revealing dose-proportional exposure of (*R*)-**24** across administered doses (10−100 mg/kg), with maximal suppression of downstream ERK phosphorylation achieved at doses as low as 30 mg/kg (Figure 6a).[26] Significantly, at this time point, the 30 mg/kg dose group showed unbound plasma and total tumor exposures (3 and 11 nM, respectively) considerably lower than the in vitro p-ERK IC_{50} (28 nM; determined after a 2 h incubation), providing an initial indication that covalent inactivation of $KRAS^{G12C}$ could have durable downstream effects, even in the absence of circulating drug.

Greatly encouraged by this result, we subsequently profiled (*R*)-**24** in a nude mouse xenograft efficacy study using the same MIA PaCa-2 T2 cell line employed in the prior study. Dosed orally once daily (10−100 mg/kg) over 2 weeks following tumor establishment, (*R*)-**24** fully suppressed tumor growth at a dose of 30 mg/kg and elicited tumor regression at doses of ≥60 mg/kg (Figure 6b).[27] A time-course PK study of (*R*)-**24** in nude mice (30 mg/kg, po) again confirmed results from our earlier PK/PD study, showing that in vivo coverage of the in vitro 2 h p-ERK IC_{50} for <2−3 h was sufficient to achieve tumor growth stasis (Figure 6c).

It came as a great disappointment to us, then, when we subsequently found crystalline polymorphic forms of (*R*)-**24** to have significantly reduced oral bioavailability (4−12%) relative to that of the amorphous form used in our earlier studies (Table 5), impairing our ability to achieve suitable plasma exposures in future studies. As reduced bioavailability coincided with dramatically reduced solubility in biorelevant media (<0.004 mg/mL (crystalline forms) vs >0.108 mg/mL (amorphous form) in FaSSGF, FaSSIF, PBS), we subsequently prioritized efforts to identify (*R*)-**24** analogues that demonstrated superior aqueous solubility. Two strategies dominated these efforts: (1) reducing the lipophilicity of (*R*)-**24** by changing the quinazolinone C6 halogen substituent and (2) increasing the polar surface area of (*R*)-**24** by introducing an additional nitrogen atom into the cryptic pocket ring (Table 5).

Initial efforts focused on nitrogen atom incorporation into the cryptic pocket ring. Replacement of the carbon atoms adjacent to the isopropyl or methyl substituents with nitrogen atoms (cf., compounds **34** and **35**, respectively) significantly enhanced aqueous solubility without appreciably altering KRAS activity. Such substitution also substantially reduced MDCK permeability, however, affording molecules with no measurable oral bioavailability (BALB/c mice). Although bis-nitrogen substitution (**36**) likewise further enhanced aqueous solubility, the resulting pyrimidine analogue similarly suffered from low permeability and no measurable oral bioavailability.

We next investigated whether reducing the lipophilicity of the quinazolinone C6 substituent could enhance aqueous solubility while preserving cellular activity. While replacing the C6 chloro substituent of (*R*)-**24** with a fluoro substituent (compound **37**) led to a modest loss of activity in cellular assays (e.g., p-ERK IC_{50} = 90 nM), the change also resulted in

DOI: 10.1021/acs.jmedchem.9b01180
J. Med. Chem. 2020, 63, 52−65

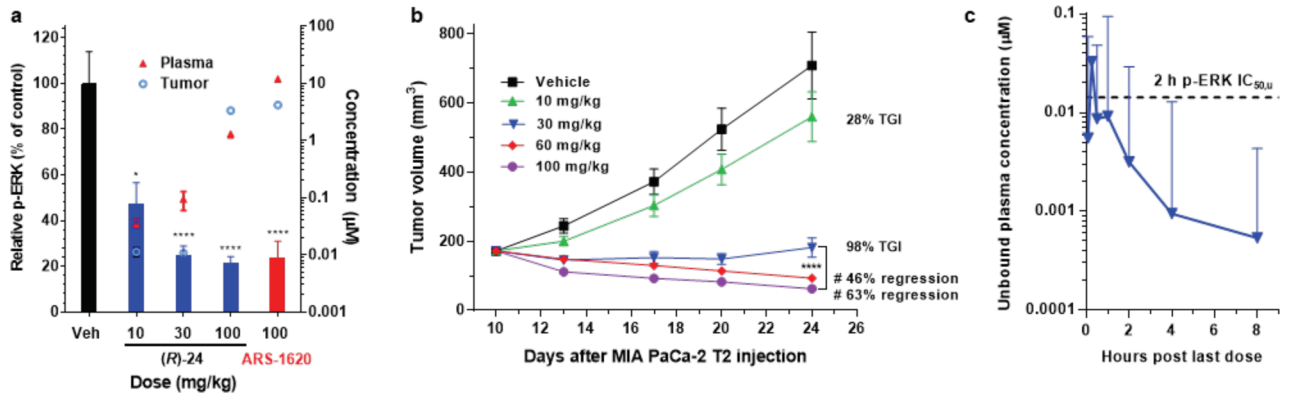

Figure 6. (*R*)-**24** inhibits ERK1/2 phosphorylation in *KRAS p.G12C* tumors (MIA PaCa-2 T2) and causes tumor regression at QD po doses of ≥60 mg/kg. (a) Mice bearing MIA PaCa-2 T2 tumors were given a single oral dose of vehicle (black bar), (*R*)-**24** (blue bars), or ARS-1620 (red bar); tumors were harvested 2 h later and assessed for p-ERK levels. Plasma and tumor concentrations of (*R*)-**24** are indicated by red triangles and blue open circles, respectively. Data are presented as percent of control versus vehicle ± SEM (n = 3/group): ****p < 0.0001; *p < 0.05 by one-way ANOVA with Dunnett's post hoc analysis. (b) Effect of (*R*)-**24** on MIA PaCa-2 T2 tumor growth in nude mice (QD po dosing). Data represent mean tumor volume ± SEM (n = 10/group): ****p < 0.0001 by RMANOVA followed by Dunnett's post hoc analysis, #p < 0.0001 regression by paired t test. (c) Mean unbound plasma concentrations + SEM (n = 3) following 30 mg/kg po dosing in nude mice. p-ERK $IC_{50,u}$ = in vitro cellular IC_{50}·$f_{u,media}$ (fraction unbound in cell culture media).

Table 5. Biopharmaceutical Optimization of (*R*)-24 Significantly Enhances Bioavailability

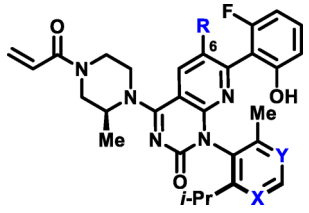

cmpd	R	X	Y	log *D* (pH 7.4)| PSA (Å^2)[a]	p-ERK IC_{50} MIA PaCa-2 (μM)[b]	viability IC_{50} MIA PaCa-2| A549 (μM)[c]	MulH hep CL_{int} ((μL/min)/10^6 cells)	MDCK permeability A−B (μcm/s)	HT solubility (μM, PBS| FaSSIF| 0.01 N HCl)	mouse CL (L h^{-1} kg^{-1})| V_{ss} (L/kg)|$t_{1/2}$ (h)| *F* (%)[d]
(*R*)-**24**	Cl	CH	CH	3.6 | 89	0.028	0.002 | 11.9	102 | 30	15	12|204|9	1.4|0.8|0.9|4−12[e]
(*R*)-**34**	Cl	N	CH	2.4 | 102	0.011	0.001 | 34.1	75 | 11	1	46|381|500	3.9|1.4|0.4|< 0.5
(*S*)-**35**[f]	Cl	CH	N	2.4 | 102	0.065	0.003 | 32.4	96 | 5	2	335|435|534	1.4|0.4|0.4|< 0.5
(*R*)-**36**	Cl	N	N	1.7 | 115	0.038	0.003 | >50	139 | 5	1	499|500|421	3.5|1.1|0.3|< 0.5
(*R*)-**37**	F	CH	CH	3.0 | 89	0.090	0.011 | 11.6	111 | 37	22	41|164|24	2.0|1.0|0.5|< 0.5
(*R*)-**38**	F	N	CH	2.0 | 102	0.068	0.005 |36.5	36 | 9	6	423|492|499	1.6|0.7|0.5|22−40
(*S*)-**39**[f]	F	CH	N	2.0 | 102	0.142	0.016 | 49.1	100 | 9	1	426|477|484	3.7|1.1|0.3|15
(*R*)-**40**	F	N	N	1.2 | 115	0.128	0.009 | >50	65 | 5	<1	495|500|500	4.7|1.7|0.3|10

[a]log *D* (pH 7.4) and PSA (polar surface area) calculated using ACD/Percepta (ACD/Labs, Toronto, Canada). [b]p-ERK1/2 immunoassay (MSD), 2 h incubation. [c]Viability assessed at 72 h by CellTiter-Glo luminescence assay (Promega) in MIA PaCa-2 (*p.G12C*) and A549 (*p.G12S*) cell lines. All data represent $n \geq 2$. [d]iv/po dosing in BALB/c mice (vehicle: iv, 1 mg/kg, DMSO; po, 10 mg/kg, 1% Tween 80, 2% HPMC, 97% water). [e]Crystalline polymorphs. [f]Presence of the pyridyl nitrogen changes IUPAC substituent priority for naming purposes; the isopropyl substituent remains oriented toward the cryptic pocket, as in other analogues.

a modest increase in aqueous solubility (~3-fold) and no adverse impact on membrane permeability (P_{AB} = 22 μcm/s). Unfortunately, (*R*)-**37** failed to show any measurable oral bioavailability (F < 0.5%). Combining C6 fluoro substitution with nitrogen incorporation in the cryptic pocket arene ring (compounds **38**−**40**), however, overcame the consistently low bioavailabilities seen with prior analogues. Although nitrogen atom incorporation again led to significantly reduced MDCK permeabilities for all three compounds, this combination of features led to dramatically enhanced aqueous solubilities (>423 μM in all biorelevant media). From these studies, (*R*)-**38** emerged as the standout molecule, showing good activity in cellular assays (p-ERK IC_{50} = 68 nM), moderate permeability (P_{AB} = 6 μcm/s), and exceptional oral bioavailability (22−40% as a crystalline form).

Gratifyingly, (*R*)-**38** demonstrated dose-proportional plasma exposure when dosed orally (0.3−100 mg/kg) in our nude mouse MIA PaCa-2 xenograft model and significantly suppressed ERK phosphorylation at doses of ≥10 mg/kg (Figure 7a).[26] To further interrogate the PK/PD relationship for (*R*)-**38**, we also conducted a time-course pharmacodynamic study in this xenograft model (Figure 7b). This study supported earlier results with (*R*)-**24** and (*R*)-**38**, showing that, while maximal suppression of ERK phosphorylation was achieved 60−120 min postdosing, peak (*R*)-**38** plasma and tumor exposures were achieved 30 min postdosing, and by the 120 min time point, only low concentrations of (*R*)-**38** remained in circulation.

A time-course study of $KRAS^{G12C}$ ligand occupancy in the MIA PaCa-2 xenograft model shed further light on this PK/PD

DOI: 10.1021/acs.jmedchem.9b01180
J. Med. Chem. 2020, 63, 52−65

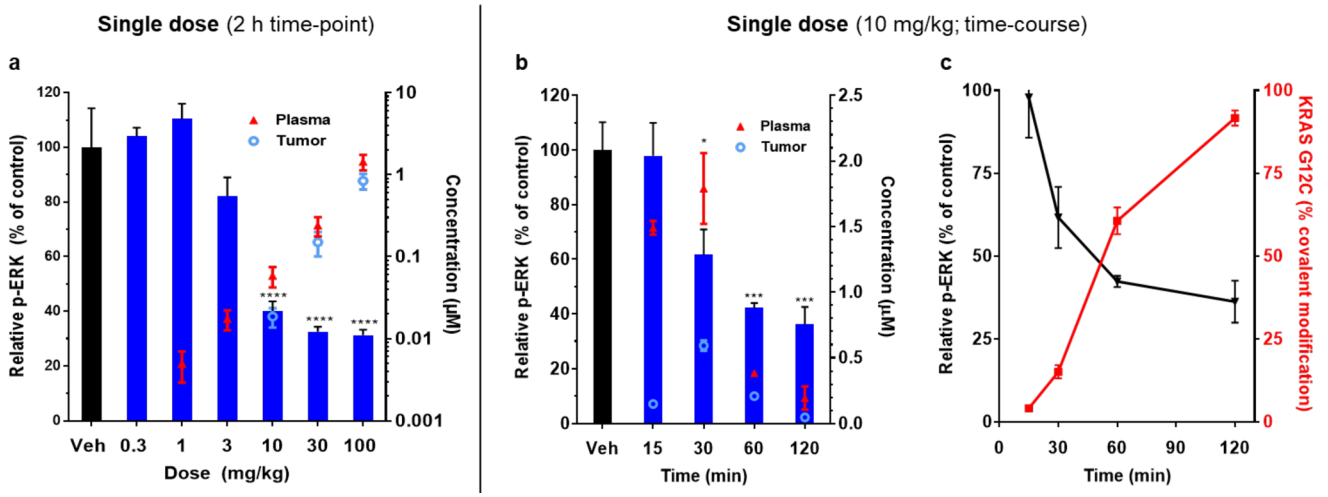

Figure 7. Data are initially published in ref 28. p-ERK (a) dose–response and (b) time-course (MSD) data with plasma and tumor exposures for compound (*R*)-**38**. Mice bearing MIA PaCa-2 T2 tumors were given a single oral dose of either vehicle (black bars) or (*R*)-**38** (blue bars) and harvested at the indicated time. Data represent percent of control versus vehicle ± SEM (n = 3/group). Plasma and tumor concentrations of (*R*)-**24** are indicated by red triangles and blue open circles, respectively: ****p < 0.0001; ***p < 0.001; *p < 0.05 by one-way ANOVA with Dunnett's post hoc analysis. (c) p-ERK POC (MSD) and percent $KRAS^{G12C}$ covalent modification (MS) time-course in MIA PaCa-2 T2 mouse xenografts. Markers represent mean p-ERK1/2 levels (percent of basal ERK1/2) ± SEM and mean % covalent modification ± SEM (n = 3/group).

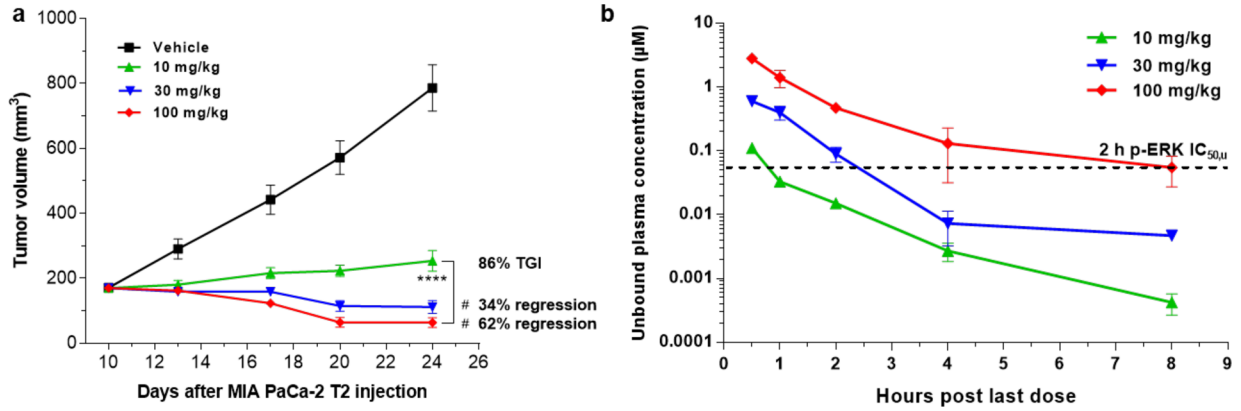

Figure 8. Data are initially published in ref 28 Compound (*R*)-**38** dosed orally once daily results in regression of *KRAS p.G12C* tumor xenografts. (a) Effect of compound (*R*)-**38** on MIA PaCa-2 T2 xenograft growth in nude mice (QD PO dosing). Data represent the mean tumor volume ± SEM (n = 10/group): ****p < 0.0001 by Dunnett's post hoc analysis; #p < 0.05 regression by paired t test. (b) Mean unbound plasma concentrations ± SEM (n = 2/group). p-ERK $IC_{50,u}$ = in vitro cellular IC_{50}·$f_{u,media}$ (fraction unbound in cell culture media).

relationship (Figure 7c). By use of protein immunocapture, trypsin digestion, and mass spectrometry, $KRAS^{G12C}$ covalent modification in tumor cells recovered from treated mice was monitored over time, revealing suppression of ERK phosphorylation to closely mirror the extent of covalent modification of $KRAS^{G12C}$.[26] Covalent modification of $KRAS^{G12C}$ was nearly complete 120 min postdosing, at which point minimal (*R*)-**38** remained in circulation.

Encouraged by these promising pharmacodynamic effects, (*R*)-**38** was profiled in a mouse xenograft efficacy study employing MIA PaCa-2 T2 (*p.G12C*) tumor cells. Once-daily oral dosing (10–100 mg/kg) achieved 86% tumor growth inhibition (TGI) at 10 mg/kg and produced significant tumor regression at doses of ≥30 mg/kg (Figure 8a). Unbound plasma exposures from this study (Figure 8b) again illustrated that durable growth responses could be achieved in the absence of continuous drug exposure given the covalent inhibitor mechanism of action. At a dose of 10 mg/kg, plasma coverage of the in vitro p-ERK IC_{50} was only sustained for ∼1 h, and circulating, unbound concentrations of (*R*)-**38** had dropped below 1 nM 8 h postdosing. Nonetheless, 1 h coverage of the in vitro p-ERK IC_{50} proved sufficient to achieve near-stasis in tumor growth, and in vitro IC_{50} coverage for as little as 2 h (30 mg/kg dose) was sufficient to cause tumor regression.

Delighted by the promising pharmacodynamic effect of (*R*)-**38** in our mouse models, we undertook further characterization of (*R*)-**38** to assess its potential as a possible development candidate. Cocrystallization with $KRAS^{G12C}$ revealed (*R*)-**38** to adopt a similar binding mode to prior quinazolinone leads, with the quinazolinone core of (*R*)-**38** occupying the KRAS switch II pocket and the acrylamide moiety making a covalent bond with C12 (Figure 9). The (*S*)-methylpiperazine ring of (*R*)-**38** adopted a twist-boat conformation, with the C2 methyl substituent making close contacts with C12 and Y96. Critically, the isopropyl substituent of the pyridyl ring again made close contacts with Y96, H95, and Q99, largely filling the cryptic pocket revealed by side chain rotation of the H95 residue and contributing to the exceptional potency of this molecule. Nitrogen substitution of the cryptic pocket arene ring was not

DOI: 10.1021/acs.jmedchem.9b01180
J. Med. Chem. 2020, 63, 52–65

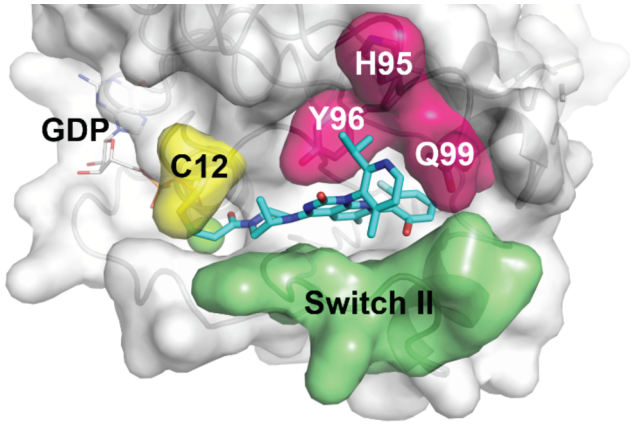

Figure 9. X-ray crystal structure of compound (*R*)-**38** bound to GDP-KRAS^{G12C} (cyan, PDB code 6OIM).

found to adversely impact the configurational stability of the potent *R*-atropisomer, which was calculated to have a racemization $t_{1/2}$ of >180 years at 25 °C ($\Delta G^{\ddagger}_{rotation}$ > 31 kcal/mol; Table 6).

Table 6. Additional in Vitro and PK Characterization of Compound (*R*)-38

atropisomer interconversion barrier ($\Delta G^{\ddagger}$, kcal/mol)[a]	>31
rat CL (L h^{-1} kg^{-1})|V_{ss} (L/kg)|$t_{1/2}$ (h)|F (%)[b]	3.4|2.0|0.5|28
dog CL (L h^{-1} kg^{-1})|V_{ss} (L/kg)|$t_{1/2}$ (h)|F (%)[c]	2.2|0.73|0.4|34
PPB Mu|R|D|Hu (0.25 μM, UC, f_u)	0.06|0.05|0.17|0.09
KRAS^{G12C} k_{inact}/K_I (M^{-1} s^{-1})[d]	9900 ± 1800
5 mM GSH $t_{1/2}$ (min)[e]	200

[a]Determined by NMR kinetic data. [b]iv/po dosing in Sprague-Dawley rat (vehicle: iv, 1 mg/kg, DMSO; po, 10 mg/kg, 1% Tween 80, 2% HPMC, 97% water). [c]iv/po dosing in Beagle dog (vehicle: iv, 1 mg/kg, 10% DMAC, 10% EtOH, 30% propylene glycol, 50% water; po, 10 mg/kg, 1% Tween 80, 2% HPMC, 97% water). [d]k_{inact}/K_I was determined from time-course relative % bound data at varied inhibitor concentrations, as assessed by mass spectrometry.[28,31] [e]$t_{1/2}$ determined by parent depletion (MS detection) in 5 mM GSH, 37 °C, pH 7.4 aqueous phosphate buffer.[32]

Rat and dog pharmacokinetic parameters for (*R*)-**38** were in line with those observed in mouse, with reasonable oral bioavailability observed in all species. Although terminal half-lives for (*R*)-**38** were relatively short in all species, this was not viewed as a liability, given our findings from prior pharmacodynamic studies that durable covalent inhibition of KRAS^{G12C} could be achieved without continuous drug exposure. Such persistent PD effects are in line with those expected for covalent inhibitors, where duration of target inhibition is determined not by the duration of target IC_{50} coverage but rather by the resynthesis rate of the covalently inactivated target protein.[29] Given KRAS's long protein half-life (~22 h),[30] rapid covalent inactivation allows for durable pharmacodynamic effects even in the face of relatively short inhibitor plasma half-lives.

Although mass spectrometric studies[31] established (*R*)-**38** to have a second-order rate constant for covalent inactivation of KRAS^{G12C} (k_{inact}/K_I) of 9900 M^{-1} s^{-1}, rapid inactivation of KRAS was not indicative of promiscuous cysteine reactivity. Incubation of (*R*)-**38** under conditions mimicking intracellular glutathione levels (5 mM GSH, 37 °C, pH 7.4)[32] revealed (*R*)-**38** to have a GSH conjugation half-life of 200 min. Cysteine-proteome profiling (MS) further revealed (*R*)-**38** to be highly selective for covalent modification of KRAS^{G12C}: of 6451 cysteine-containing peptides profiled, only the KRAS^{G12C} C12 peptide was found to be significantly modified .[28]

On the basis of the compelling pharmacological profile of (*R*)-**38** and its marked ability to regress *KRAS p.G12C* mutant tumors in vivo, its promising biopharmaceutical properties, and its excellent tolerability in preclinical toxicological models,[33] we nominated (*R*)-**38** for clinical development as AMG 510. AMG 510 entered human clinical trials in August 2018, and a phase I/II trial evaluating its safety, tolerability, pharmacokinetic properties, and efficacy in *KRAS p.G12C* mutant tumors is currently ongoing (NCT03600883[34]). Early results from this study have confirmed AMG 510 to demonstrate excellent tolerability and promising antitumor activity when administered as a monotherapy to patients with advanced *KRAS p.G12C* mutant solid tumors.[35] Dose-expansion efforts are currently ongoing.

CONCLUSIONS

By exploiting a previously unrecognized H95/Y96/Q99 cryptic pocket in GDP-KRAS^{G12C}, we were able to create highly potent and selective covalent inhibitors of KRAS^{G12C}. A collaboration with Carmot Therapeutics[7] enabled us to rapidly screen cysteine-reactive libraries and investigate the potential of this cryptic pocket. Structure-based design efforts facilitated our discovery of a quinazolinone-based scaffold, which exploited this pocket for enhanced potency and provided ADME properties suitable for further optimization. Optimally leveraging the H95/Y96/Q99 cryptic pocket required us to address axial chirality and configurational stability issues, which were overcome by optimization of the cryptic pocket-engaging arene moiety. Further refinement of the resulting leads to address permeability, solubility, and oral bioavailability challenges then led to our discovery of AMG 510. AMG 510 has shown great promise in the treatment of *KRAS p.G12C* mutant tumors both preclinically and clinically. Efforts to further demonstrate the clinical potential of AMG 510 are currently underway.

EXPERIMENTAL SECTION

General Synthetic Procedures. All materials were obtained from commercial suppliers and used without further purification unless otherwise noted. Anhydrous solvents were obtained from Sigma-Aldrich and used directly. Reactions involving air- or moisture-sensitive reagents were performed under a nitrogen or argon atmosphere. Silica gel chromatography was performed using prepacked silica gel cartridges (RediSep Rf, Teledyne ISCO). Reverse-phase HPLC purification was performed using Gilson (Middleton, WI) workstations. NMR spectra were acquired on Bruker Avance 400, 500, and 600 MHz spectrometers equipped with 5 mm BBFO probes. All final compounds were purified to >95% purity as determined by LC–MS using an Agilent 1100 or 1260 multiwavelength detector (215 nm detection) and an Advanced Materials Technology HALO C18 column (50 mm × 3.0 mm, 2.7 μm) at 40 °C with a 2.0 mL/min flow rate using a 5–95% gradient of acetonitrile/water with 0.1% trifluoracetic acid over 1.5 min. Low-resolution MS data were obtained concurrently with UV chromatography using an Agilent G1956B MSD SL, 6120B, 6130B, or 6140A quadrupole MS in positive electrospray ionization mode. Resolved atropisomers were purified to >95% ee (or de) using a Thar 80, 200, or 350 preparative SFC. Enantiomeric and diastereomeric excesses were determined by SFC (Waters Acquity UPC2 or Agilent 1260 Infinity analytical systems).

DOI: 10.1021/acs.jmedchem.9b01180
J. Med. Chem. 2020, 63, 52–65

Synthesis of AMG 510 [(*R*)-38]. Step 1. 2,6-Dichloro-5-fluoronicotinamide. Oxalyl chloride (2 M solution in DCM, 11.9 mL, 23.8 mmol) and DMF (0.05 mL) were sequentially added to 2,6-dichloro-5-fluoronicotinic acid (4.0 g, 19.1 mmol, AstaTech, Inc.) in DCM (48 mL), and the resulting mixture was stirred at ambient temperature for 16 h. The reaction mixture was then concentrated in vacuo, and the residue was dissolved in 1,4-dioxane (48 mL) and cooled to 0 °C. Ammonium hydroxide solution (28−30% NH_3 basis, 3.6 mL, 28.6 mmol) was slowly added, and the resulting mixture was stirred at 0 °C for 30 min. The mixture was then concentrated in vacuo, and the residue was diluted with 1:1 EtOAc/heptane, agitated for 5 min, and filtered. The filtrate was concentrated to half-volume and refiltered. The combined collected solids were washed with heptane and dried overnight in a reduced-pressure oven (45 °C) to provide 2,6-dichloro-5-fluoronicotinamide (2.0 g, 50% yield). ^{1}H NMR (400 MHz, DMSO-d_6) δ 8.23 (d, J = 7.9 Hz, 1 H) 8.09 (br s, 1 H) 7.93 (br s, 1 H). ^{19}F NMR (376 MHz, DMSO-d_6) δ: − 122.39 (s, 1 F). m/z (ESI, +ve ion): 208.9 $(M + H)^+$.

Step 2. 2,6-Dichloro-5-fluoro-*N*-((2-isopropyl-4-methylpyridin-3-yl)carbamoyl)nicotinamide. To an ice-cooled slurry of 2,6-dichloro-5-fluoronicotinamide (5.0 g, 23.9 mmol) in THF (20 mL) was slowly added oxalyl chloride (2 M solution in DCM, 14.4 mL, 28.8 mmol). The resulting mixture was stirred at 75 °C for 1 h, then allowed to cool and concentrated in vacuo to half volume. The concentrate was cooled to 0 °C and diluted with THF (20 mL). A solution of 2-isopropyl-4-methylpyridin-3-amine (3.59 g, 23.9 mmol) in THF (10 mL) was added dropwise via cannula. The resulting mixture was stirred at 0 °C for 1 h, diluted with a 1:1 mixture of brine and saturated aqueous ammonium chloride, and extracted with EtOAc (3×). The combined organic extracts were dried over anhydrous sodium sulfate and concentrated in vacuo to provide 2,6-dichloro-5-fluoro-*N*-((2-isopropyl-4-methylpyridin-3-yl)carbamoyl)-nicotinamide, which was used without further purification. m/z (ESI, +ve ion): 385.1 $(M + H)^+$.

Intermediate, Step 2. 2-Isopropyl-4-methylpyridin-3-amine. To a slurry of 3-amino-2-bromo-4-picoline (360 mg, 1.9 mmol; Combi-Blocks, Inc.) in THF (4 mL) was added [1,1′-bis(diphenylphosphino)ferrocene]dichloropalladium(II), complex with DCM (79 mg, 0.10 mmol). The resulting slurry was deoxygenated with argon, then 2-propylzinc bromide (0.5 M solution in THF, 5.4 mL, 2.7 mmol) was added. The resulting solution was stirred at 60 °C for 17 h, then the reaction was allowed to cool to ambient temperature. Water (10 mL) and 1 N NaOH solution (20 mL) were sequentially added, and the resulting mixture was extracted with EtOAc (2×). The combined organic extracts were dried over anhydrous sodium sulfate and concentrated in vacuo. Chromatographic purification of the residue (silica gel; 0−15% MeOH/DCM) provided 2-isopropyl-4-methylpyridin-3-amine (284 mg, 98% yield) as a brown solid. ^{1}H NMR (400 MHz, DMSO-d_6) δ ppm 7.66 (d, J = 4.6 Hz, 1 H), 6.78 (d, J = 4.8 Hz, 1 H), 4.72 (br s, 2 H), 3.14−3.25 (m, 1 H), 2.08 (s, 3 H), 1.14 (d, J = 6.8 Hz, 6 H). m/z (ESI, +ve ion): 151.1 $(M + H)^+$.

Step 3. 7-Chloro-6-fluoro-1-(2-isopropyl-4-methylpyridin-3-yl)pyrido[2,3-*d*]pyrimidine-2,4(1*H*,3*H*)-dione. To an ice-cooled solution of 2,6-dichloro-5-fluoro-*N*-((2-isopropyl-4-methylpyridin-3-yl)carbamoyl)nicotinamide (9.2 g, 24.0 mmol) in THF (40 mL) was slowly added KHMDS (1 M solution in THF, 50.2 mL, 50.2 mmol). The ice bath was removed, and the resulting mixture was stirred for 40 min at ambient temperature. Saturated aqueous ammonium chloride solution was added, and the resulting mixture was extracted with EtOAc (3×). The combined organic extracts were dried over anhydrous sodium sulfate and concentrated in vacuo. Chromatographic purification of the residue (silica gel; 0−50% 3:1 EtOAc−EtOH/heptane) provided 7-chloro-6-fluoro-1-(2-isopropyl-4-methylpyridin-3-yl)pyrido[2,3-*d*]pyrimidine-2,4(1*H*,3*H*)-dione (9.24 g, quantitative yield). ^{1}H NMR (400 MHz, DMSO-d_6) δ 12.27 (br s, 1 H), 8.48−8.55 (m, 2 H), 7.29 (d, J = 4.8 Hz, 1 H), 2.87 (quin, J = 6.6 Hz, 1 H), 1.99−2.06 (m, 3 H), 1.09 (d, J = 6.6 Hz, 3 H), 1.01 (d, J = 6.6 Hz, 3 H). ^{19}F NMR (376 MHz, DMSO-d_6) δ −126.90 (s, 1 F). m/z (ESI, +ve ion): 349.1 $(M + H)^+$.

Step 4. 4,7-Dichloro-6-fluoro-1-(2-isopropyl-4-methylpyridin-3-yl)pyrido[2,3-*d*]pyrimidin-2(1*H*)-one. Phosphorus oxychloride (1.63 mL, 17.5 mmol) was added, dropwise, to a solution of 7-chloro-6-fluoro-1-(2-isopropyl-4-methylpyridin-3-yl)pyrido[2,3-*d*]pyrimidine-2,4(1*H*,3*H*)-dione (4.7 g, 13.5 mmol) and DIPEA (3.5 mL, 20 mmol) in acetonitrile (20 mL), and the resulting mixture was stirred at 80 °C for 1 h, then cooled to ambient temperature and concentrated in vacuo to provide 4,7-dichloro-6-fluoro-1-(2-isopropyl-4-methylpyridin-3-yl)pyrido[2,3-*d*]pyrimidin-2(1*H*)-one, which was used without further purification. m/z (ESI, +ve ion): 367.1 $(M + H)^+$.

Step 5. (*S*)-*tert*-Butyl 4-(7-Chloro-6-fluoro-1-(2-isopropyl-4-methylpyridin-3-yl)-2-oxo-1,2-dihydropyrido[2,3-*d*]pyrimidin-4-yl)-3-methylpiperazine-1-carboxylate. To an ice-cooled solution of 4,7-dichloro-6-fluoro-1-(2-isopropyl-4-methylpyridin-3-yl)-pyrido[2,3-*d*]pyrimidin-2(1*H*)-one (13.5 mmol) in acetonitrile (20 mL) was added DIPEA (7.1 mL, 40.3 mmol) followed by (*S*)-4-Boc-2-methylpiperazine (3.23 g, 16.1 mmol, Combi-Blocks, Inc.). The resulting mixture was warmed to ambient temperature and stirred for 1 h, then diluted with cold saturated aqueous sodium bicarbonate solution (200 mL) and EtOAc (300 mL). The mixture was stirred for an additional 5 min, and the organic layer was collected. The aqueous layer was extracted with additional EtOAc (1×), and the combined organic extracts were dried over anhydrous sodium sulfate and concentrated in vacuo. Chromatographic purification of the residue (silica gel; 0−50% EtOAc/heptane) gave (*S*)-*tert*-butyl 4-(7-chloro-6-fluoro-1-(2-isopropyl-4-methylpyridin-3-yl)-2-oxo-1,2-dihydropyrido-[2,3-*d*]pyrimidin-4-yl)-3-methylpiperazine-1-carboxylate (5.71 g, 80% yield). ^{1}H NMR (400 MHz, DMSO-d_6) δ 8.45−8.51 (1 H, m), 8.31−8.41 (1 H, m), 7.23−7.29 (1 H, m), 4.67−5.01 (1 H, m), 4.09−4.25 (1 H, m), 3.88−4.07 (1 H, m), 3.78−3.87 (1 H, m), 3.59−3.74 (1 H, m), 3.04−3.21 (2 H, m), 2.59−2.66 (1 H, m), 1.88−1.98 (3 H, m), 1.43−1.50 (9 H, m), 1.27−1.35 (3 H, m), 1.03−1.10 (3 H, m), 0.94−1.03 (3 H, m). m/z (ESI, +ve ion): 531.2 $(M + H)^+$.

Step 6. (3*S*)-*tert*-Butyl 4-(6-Fluoro-7-(2-fluoro-6-hydroxyphenyl)-1-(2-isopropyl-4-methylpyridin-3-yl)-2-oxo-1,2-dihydropyrido[2,3-*d*]pyrimidin-4-yl)-3-methylpiperazine-1-carboxylate. A mixture of (*S*)-*tert*-butyl 4-(7-chloro-6-fluoro-1-(2-isopropyl-4-methylpyridin-3-yl)-2-oxo-1,2-dihydropyrido[2,3-*d*]-pyrimidin-4-yl)-3-methylpiperazine-1-carboxylate (4.3 g, 8.1 mmol), (2-fluoro-6-hydroxyphenyl)potassium trifluoroborate (2.9 g, 10.5 mmol), potassium acetate (3.2 g, 32.4 mmol), and [1,1′-bis-(diphenylphosphino)ferrocene]dichloropalladium(II) complex with dichloromethane (661 mg, 0.81 mmol) in 1,4-dioxane (80 mL) was sparged with nitrogen for 1 min. Deoxygenated water (14 mL) was added, and the resulting mixture was heated at 90 °C for 1 h, then cooled to ambient temperature, diluted with half-saturated aqueous sodium bicarbonate, and sequentially extracted with EtOAc (2×) and DCM (1×). The combined organic extracts were dried over anhydrous sodium sulfate and concentrated in vacuo. Chromatographic purification of the residue (silica gel; 0−60% 3:1 EtOAc−EtOH/heptane) furnished (3*S*)-*tert*-butyl 4-(6-fluoro-7-(2-fluoro-6-hydroxyphenyl)-1-(2-isopropyl-4-methylpyridin-3-yl)-2-oxo-1,2-dihydropyrido[2,3-*d*]pyrimidin-4-yl)-3-methylpiperazine-1-carboxylate (4.52 g, 92% yield). ^{1}H NMR (400 MHz, DMSO-d_6) δ 10.19 (br s, 1 H), 8.38 (d, J = 5.0 Hz, 1 H), 8.26 (dd, J = 12.5, 9.2 Hz, 1 H), 7.23−7.28 (m, 1 H), 7.18 (d, J = 5.0 Hz, 1 H), 6.72 (d, J = 8.0 Hz, 1 H), 6.68 (t, J = 8.9 Hz, 1 H), 4.77−4.98 (m, 1 H), 4.24 (br t, J = 14.2 Hz, 1 H), 3.93−4.08 (m, 1 H), 3.84 (br d, J = 12.9 Hz, 1 H), 3.52−3.75 (m, 1 H), 3.07−3.28 (m, 1 H), 2.62−2.74 (m, 1 H), 1.86−1.93 (m, 3 H), 1.43−1.48 (m, 9 H), 1.35 (dd, J = 10.8, 6.8 Hz, 3 H), 1.26−1.32 (m, 1 H), 1.07 (dd, J = 6.6, 1.7 Hz, 3 H), 0.93 (dd, J = 6.6, 2.1 Hz, 3 H). ^{19}F NMR (376 MHz, DMSO-d_6) δ −115.6 (s, 1 F), −128.6 (s, 1 F). m/z (ESI, +ve ion): 607.3 $(M + H)^+$.

Intermediate, Step 6. (2-Fluoro-6-hydroxyphenyl)potassium Trifluoroborate. A solution of potassium fluoride (44.7 g, 770 mmol) in water (75 mL) was added to a suspension of (2-fluoro-6-hydroxyphenyl)boronic acid (30 g, 192 mmol, Combi-Blocks, Inc.) in acetonitrile (750 mL). After 2 min of stirring, a solution of L-(+)-tartaric acid (72.2 g, 481 mmol) in THF (375 mL) was added

DOI: 10.1021/acs.jmedchem.9b01180
J. Med. Chem. 2020, 63, 52−65

over 10 min. The resulting mixture was mechanically stirred for 1 h. Suspended solids were removed by filtration and washed with a small amount of THF. The combined filtrate was then partially concentrated in vacuo until solids began to precipitate. The filtrate was cooled to −20 °C and stirred for 16 h, then slowly warmed to ambient temperature. 2-Propanol (20 mL) was added, and the precipitated solid was collected by filtration and washed with 2-propanol to provide 27.5 g of solid. The filtrate was again partially concentrated (until precipitation was observed), cooled to −20 °C, and stirred for 20 min. Additional 2-propanol was added, and the precipitated solid was collected by filtration and washed with 2-propanol. The two batches of solid were combined to provide (2-fluoro-6-hydroxyphenyl)potassium trifluoroborate (34.6 g, 82% yield). ^{1}H NMR (400 MHz, DMSO-d_6) δ 8.07 (q, J = 14.7 Hz, 1 H), 6.93 (q, J = 7.5 Hz, 1 H), 6.30−6.38 (m, 2 H).

AMG 510 [(*R*)-38]. (1*R*)-6-Fluoro-7-(2-fluoro-6-hydroxyphenyl)-1-[4-methyl-2-(1-methylethyl)-3-pyridinyl]-4-[(2*S*)-2-methyl-4-(1-oxo-2-propen-1-yl)-1-piperazinyl]-pyrido[2,3-*d*]-pyrimidin-2(1*H*)-one. Trifluoroacetic acid (25 mL, 320 mmol) was added to a solution of (3*S*)-*tert*-butyl 4-(6-fluoro-7-(2-fluoro-6-hydroxyphenyl)-1-(2-isopropyl-4-methylpyridin-3-yl)-2-oxo-1,2-dihydropyrido[2,3-*d*]pyrimidin-4-yl)-3-methylpiperazine-1-carboxylate (6.3 g, 10 mmol) in DCM (30 mL), and the resulting mixture was stirred at ambient temperature for 1 h. The mixture was then concentrated in vacuo, and the residue was taken up in DCM (30 mL), cooled to 0 °C, and sequentially treated with DIPEA (7.3 mL, 42 mmol) and a solution of acryloyl chloride (0.849 mL, 10.4 mmol) in DCM (3 mL; added dropwise). The resulting mixture was stirred at 0 °C for 10 min, then diluted with half-saturated aqueous sodium bicarbonate and extracted with DCM (2×). The combined extracts were dried over anhydrous sodium sulfate and concentrated in vacuo. Chromatographic purification of the residue (silica gel; 0−100% 3:1 EtOAc−EtOH/heptane) followed by chiral supercritical fluid chromatography (Chiralpak IC, 30 mm × 250 mm, 5 μm, 55% MeOH/CO_2, 120 mL/min, 102 bar) provided (1*R*)-6-fluoro-7-(2-fluoro-6-hydroxyphenyl)-1-[4-methyl-2-(1-methylethyl)-3-pyridinyl]-4-[(2*S*)-2-methyl-4-(1-oxo-2-propen-1-yl)-1-piperazinyl]pyrido[2,3-*d*]pyrimidin-2(1*H*)-one (AMG 510; (*R*)-**38**; 2.25 g, 43% yield) as the first-eluting peak. ^{1}H NMR (600 MHz, DMSO-d_6) δ ppm 10.20 (s, 1H), 8.39 (d, J = 4.9 Hz, 1H), 8.30 (d, J = 8.9 Hz, 0.5H), 8.27 (d, J = 8.7 Hz, 0.5H), 7.27 (q, J = 8.4 Hz, 1H), 7.18 (d, J = 4.9 Hz, 1H), 6.87 (dd, J = 16.2, 10.8 Hz, 0.5H), 6.84 (dd, J = 16.2, 10.7 Hz, 0.5H), 6.74 (d, J = 8.4 Hz, 1H), 6.68 (t, J = 8.4 Hz, 1H), 6.21 (d, J = 16.2 Hz, 0.5H), 6.20 (d, J = 16.2 Hz, 0.5H), 5.76 (d, J = 10.8 Hz, 0.5H), 5.76 (d, J = 10.7 Hz, 0.5H), 4.91 (m, 1H), 4.41 (d, J = 12.2 Hz, 0.5H), 4.33 (d, J = 12.2 Hz, 1H), 4.28 (d, J = 12.2 Hz, 0.5H), 4.14 (d, J = 12.2 Hz, 0.5H), 4.02 (d, J = 13.6 Hz, 0.5H), 3.69 (m, 1H), 3.65 (d, J = 13.6 Hz, 0.5H), 3.52 (t, J = 12.2 Hz, 0.5H), 3.27 (d, J = 12.2 Hz, 0.5H), 3.15 (t, J = 12.2 Hz, 0.5H), 2.72 (m, 1H), 1.90 (s, 3H), 1.35 (d, J = 6.7 Hz, 3H), 1.08 (d, J = 6.7 Hz, 3H), 0.94 (d, J = 6.7 Hz, 3H). ^{19}F NMR (376 MHz, DMSO-d_6) δ −115.6 (d, J = 5.2 Hz, 1 F), −128.6 (br s, 1 F). ^{13}C NMR (151 MHz, DMSO-d_6) δ ppm 165.0 (1C), 163.4 (1C), 162.5 (1C), 160.1 (1C), 156.8 (1C), 153.7 (1C), 151.9 (1C), 149.5 (1C), 148.3 (1C), 145.2 (1C), 144.3 (1C), 131.6 (1C), 130.8 (1C), 127.9 (0.5C), 127.9 (0.5C), 127.8 (0.5C), 127.7 (0.5C), 123.2 (1C), 122.8 (1C), 111.7 (1C), 109.7 (1C), 105.7 (1C), 105.3 (1C), 51.4 (0.5C), 51.0 (0.5C), 48.9 (0.5C), 45.4 (0.5C), 44.6 (0.5C), 43.7 (0.5C), 43.5 (0.5C), 41.6 (0.5C), 29.8 (1C), 21.9 (1C), 21.7 (1C), 17.0 (1C), 15.5 (0.5C), 14.8 (0.5C). FTMS (ESI) m/z: [M + H]$^+$ calcd for $C_{30}H_{30}F_2N_6O_3$ 561.24202. Found 561.24150.

■ ASSOCIATED CONTENT

Supporting Information

The Supporting Information is available free of charge at https://pubs.acs.org/doi/10.1021/acs.jmedchem.9b01180.

Experimental details for in vitro and in vivo studies, additional crystallographic data for compounds **2** and **9**, and synthetic procedures for compounds **2**−**40** (PDF)

Molecular formula strings and some data (CSV)

Accession Codes

Atomic coordinates for the X-ray structures of compound **2** (PDB code 6PGO) and compound **9** (PDB 6PGP) bound to GDP-KRAS^{G12C} are available from the RCSB Protein Data Bank (www.rcsb.org).

■ AUTHOR INFORMATION

Corresponding Author

*Phone: (805) 313-5777. E-mail: blanman@amgen.com.

ORCID

Brian A. Lanman: 0000-0002-8768-7188
Youngsook Shin: 0000-0003-3866-354X
Hui-Ling Wang: 0000-0003-2748-5266
Ryan P. Wurz: 0000-0003-1413-5208
Michael D. Bartberger: 0000-0002-5167-3139
Douglas A. Whittington: 0000-0002-5946-8543
Victor J. Cee: 0000-0002-7714-397X

Author Contributions

The manuscript was prepared by B.A.L. with contributions from all authors.

Notes

The authors declare the following competing financial interest(s): All authors are employees/former employees of Amgen, Inc. and may hold stock in the same. All studies were funded by Amgen, Inc.

■ ACKNOWLEDGMENTS

These discovery efforts were critically enabled by the support of a diverse set of talented teams, functional leaders, and highly motivated scientists, without whom this work would not have been possible. Special thanks are extended to Larry Miller, Wes Barnhart, Heather Eastwood, and Shannon Rumfelt for their crucial assistance with the chiral and achiral purification of project leads and intermediates. Thanks are extended to David Bauer, Jim Brown, Rob Rzasa, and Ted Judd for their efforts in the initial synthetic scale-up of AMG 510 and to Rajiv Kapoor and the Syngene Amgen Research Collaboration (SARC) for their support in supplying key intermediates. Our thanks are extended to Roman Shimanovich, Prashant Agarwal, and Melanie Cooke for their pharmaceutics and formulation support. We also thank Crystallographic Consulting, LLC and the Advanced Light Source staff at beamline 5.0.2 for data collection and their support. The Berkeley Center for Structural Biology is supported in part by the National Institutes of Health, National Institute of General Medical Sciences, and the Howard Hughes Medical Institute. The Advanced Light Source is supported by the Director, Office of Science, Office of Basic Energy Sciences, of the U.S. Department of Energy under Contract DE-AC02-05CH11231. We also acknowledge the Southeast Regional Collaborative Access Team (SER-CAT) 22-ID beamline at the Advanced Photon Source, Argonne National Laboratory for data collection and support. SER-CAT is supported by its member institutions and equipment grants (S10_RR25528 and S10_RR028976) from the National Institutes of Health. Use of the Advanced Photon Source was supported by the U.S. Department of Energy, Office of Science, Office of Basic Energy Sciences, under Contract W-31-109-Eng-38. Figures were generated using The PyMOL Molecular Graphics System, version 2.2.0, Schrödinger, LLC.

DOI: 10.1021/acs.jmedchem.9b01180
J. Med. Chem. 2020, 63, 52−65

ABBREVIATIONS USED

KRAS, Kirsten rat sarcoma virus oncogene; GDP, guanosine diphosphate; GTP, guanosine triphosphate; S-IIP, switch II pocket; SOS1, son of sevenless homolog 1 protein; c-RAF, rapidly accelerated fibrosarcoma kinase (cellular homolog); p-ERK, phosphorylated extracellular signal-regulated kinase; MSD, Meso Scale Diagnostics; EGF, epidermal growth factor; PK, pharmacokinetic; MDCK, Madin–Darby canine kidney cell; iv, intravenous; po, per os (oral); SAR, structure–activity relationship; QD, quaque die (once daily); TGI, tumor growth inhibition; FaSSGF, fasted-state simulated gastric fluid; FaSSIF, fasted-state simulated intestinal fluid; PBS, phosphate buffered saline; MS, mass spectrometry; GSH, glutathione

REFERENCES

(1) Cox, A. D.; Fesik, S. W.; Kimmelman, A. C.; Luo, J.; Der, C. J. Drugging the Undruggable RAS: Mission Possible? *Nat. Rev. Drug Discovery* **2014**, *13*, 828–851.

(2) Hobbs, G. A.; Der, C. J.; Rossman, K. L. RAS Isoforms and Mutations in Cancer at a Glance. *J. Cell Sci.* **2016**, *129*, 1287–1292.

(3) Prior, I. A.; Lewis, P. D.; Mattos, C. A Comprehensive Survey of Ras Mutations in Cancer. *Cancer Res.* **2012**, *72*, 2457–2467.

(4) Holderfield, M. Efforts to Develop KRAS Inhibitors. *Cold Spring Harbor Perspect. Med.* **2018**, *8*, a031864.

(5) Ostrem, J. M.; Peters, U.; Sos, M. L.; Wells, J. A.; Shokat, K. M. K-Ras(G12C) Inhibitors Allosterically Control GTP Affinity and Effector Interactions. *Nature* **2013**, *503*, 548–551.

(6) Janes, M. R.; Zhang, J.; Li, L.-S.; Hansen, R.; Peters, U.; Guo, X.; Chen, Y.; Babbar, A.; Firdaus, S. J.; Darjania, L.; Feng, J.; Chen, J. H.; Li, S.; Li, S.; Long, Y. O.; Thach, C.; Liu, Y.; Zarieh, A.; Ely, T.; Kucharski, J. M.; Kessler, L. V.; Wu, T.; Yu, K.; Wang, Y.; Yao, Y.; Deng, X.; Zarrinkar, P. P.; Brehmer, D.; Dhanak, D.; Lorenzi, M. V.; Hu-Lowe, D.; Patricelli, M. P.; Ren, P.; Liu, Y. Targeting KRAS Mutant Cancers with a Covalent G12C-Specific Inhibitor. *Cell* **2018**, *172*, 578–589.

(7) Shin, Y.; Jeong, J. W.; Wurz, R. P.; Achanta, P.; Arvedson, T.; Bartberger, M. D.; Campuzano, I. D. G.; Fucini, R.; Hansen, S. K.; Ingersoll, J.; Iwig, J.; Lipford, J. R.; Ma, V.; Kopecky, D. J.; McCarter, J.; San Miguel, T.; Mohr, C.; Sabet, S.; Saiki, A. Y.; Sawayama, A.; Sethofer, S.; Tegley, C. M.; Volak, L. P.; Yang, K.; Lanman, B. A.; Erlanson, D. A.; Cee, V. J. Discovery of *N*-(1-Acryloylazetidin-3-yl)-2-(1*H*-indol-1-yl)acetamides as a Covalent Inhibitor of KRAS^{G12C}. *ACS Med. Chem. Lett.* **2019**, *10*, 1302–1308.

(8) Patricelli, M. P.; Janes, M. R.; Li, L.-S.; Hansen, R.; Peters, U.; Kessler, L. V.; Chen, Y.; Kucharski, J. M.; Feng, J.; Ely, T.; Chen, J. H.; Firdaus, S. J.; Babbar, A.; Ren, P.; Liu, Y. Selective Inhibition of Oncogenic KRAS Output with Small Molecules Targeting the Inactive State. *Cancer Discovery* **2016**, *6*, 316–329.

(9) Janes, M. R.; Zhang, J.; Li, L.-S.; Hansen, R.; Peters, U.; Guo, X.; Chen, Y.; Babbar, A.; Firdaus, S. J.; Darjania, L.; Feng, J.; Chen, J. H.; Li, S.; Li, S.; Long, Y. O.; Thach, C.; Liu, Y.; Zarieh, A.; Ely, T.; Kucharski, J. M.; Kessler, L. V.; Wu, T.; Yu, K.; Wang, Y.; Yao, Y.; Deng, X.; Zarrinkar, P. P.; Brehmer, D.; Dhanak, D.; Lorenzi, M. V.; Hu-Lowe, D.; Patricelli, M. P.; Ren, P.; Liu, Y. Targeting KRAS Mutant Cancers with a Covalent G12C-Specific Inhibitor. *Cell* **2018**, *172*, 578–589.

(10) Hansen, S.; Erlanson, D.; Cancilla, M. Methods of Chemotype Evolution. U.S. Patent 10,107,798, October 23, 2018.

(11) For independent identification of the H95/Y96/Q99 groove from a KRAS M72C screen, see Gentile, D. R.; Rathinaswamy, M. K.; Jenkins, M. L.; Moss, S. M.; Siempelkamp, B. D.; Renslo, A. R.; Burke, J. E.; Shokat, K. M. Ras Binder Induces a Modified Switch-II Pocket in GTP and GDP States. *Cell Chem. Biol.* **2017**, *24*, 1455–1466.

(12) It should be noted that covalent inhibitors derive their potency not only from noncovalent protein binding affinity (which facilitates protein–ligand preassociation) but also from features of the protein–ligand complex that accelerate covalent bond formation. Improved ligand "potencies" as described in this manuscript should be understood as arising from varying contributions of these two factors.

(13) For details, see https://www.perkinelmer.com/Content/RelatedMaterials/Brochures/BRO_AlphaScreen2004.pdf (accessed Sep 7, 2019).

(14) For details, see https://www.mesoscale.com/en/products/phospho-total-erk1-2-whole-cell-lysate-kit-k15107d/ (accessed Sep 7, 2019).

(15) A 5 min incubation represented the shortest incubation time that could be practically executed.

(16) A 2 h incubation was estimated to be the minimum time required to achieve "complete" (~95%) covalent modification of KRAS^{G12C} based on the GTP hydrolysis rate reported in ref 8.

(17) Possible reasons for the increased activity of compound **9** include more optimal orientation of the isopropylphenyl substituent in the cryptic pocket (a B3LYP/6-31G* quantum mechanical model predicts compound **8** to adopt a ground-state biaryl torsion angle of 65°, whereas the quinazolinone and phenyl rings are nearly perpendicular in compound **9**, enhancing contacts with the cryptic pocket residues) and enhanced contacts between the quinazolinone carbonyl group and proximal protein residues and water molecules.

(18) For IUPAC naming conventions, see Moss, G. P. Basic Terminology of Stereochemistry (IUPAC Recommendations 1996). *Pure Appl. Chem.* **1996**, *68*, 2193–2222.

(19) (*R*)-**9** was ~20-fold more potent than (*S*)-**9** in the ERK phosphorylation assay (MSD, 4 h incubation).

(20) For details, see https://www.promega.com/products/cell-health-assays/cell-viability-and-cytotoxicity-assays/celltiter_glo-luminescent-cell-viability-assay/?catNum=G7570 (accessed Sep 7, 2019).

(21) Intramolecular hydrogen bonding has previously been demonstrated to enhance passive membrane permeability: Rezai, T.; Bock, J. E.; Zhou, M. V.; Kalyanaraman, C.; Lokey, R. S.; Jacobson, M. P. Conformational Flexibility, Internal Hydrogen Bonding, and Passive Membrane Permeability: Successful In Silico Prediction of the Relative Permeabilities of Cyclic Peptides. *J. Am. Chem. Soc.* **2006**, *128*, 14073–14080.

(22) Atropisomer interconversion was monitored by ^{1}H NMR. Exchange rates were calculated from line-shape analysis, coalescence temperatures, or half-lives. Free energy barriers ($\Delta G^{\ddagger}$) were calculated from exchange rates using Eyring's equation. For details, see Claridge, T. D. W. *High-Resolution NMR Techniques in Organic Chemistry*, 3rd ed.; Elsevier: Amsterdam, The Netherlands, 2016; p 50.

(23) Laplante, S. R.; Fader, L. D.; Fandrick, K. R.; Fandrick, D. R.; Hucke, O.; Kemper, R.; Miller, S. P.; Edwards, P. J. Assessing Atropisomer Axial Chirality in Drug Discovery and Development. *J. Med. Chem.* **2011**, *54*, 7005–7022.

(24) Rotzler, J.; Gsellinger, H.; Bihlmeier, A.; Gantenbein, M.; Vonlanthen, D.; Häussinger, D.; Klopper, W.; Mayor, M. Atropisomerization of di-*para*-Substituted Propyl-Bridged Biphenyl Cyclophanes. *Org. Biomol. Chem.* **2013**, *11*, 110–118.

(25) In vitro p-ERK IC_{50} values were derived from EGF-stimulated MIA PaCa-2 cells.

(26) Residual ERK phosphorylation (~30%) is attributable to nonmutant KRAS activity resulting from stromal contamination of the clonal *KRAS p.G12C* tumors (confirmed by RNA-seq) and is observed both at later time points and at higher doses.

(27) No significant body weight loss was observed at any dose level in this study.

(28) Data initially published in Canon, J.; Rex, K.; Saiki, A. Y.; Mohr, C.; Cooke, K.; Bagal, D.; Gaida, K.; Holt, T.; Knutson, C. G.; Koppada, N.; Lanman, B. A.; Werner, J.; Rapaport, A. S.; San Miguel, T.; Ortiz, R.; Osgood, T.; Sun, J.-R.; Zhu, X.; McCarter, J. D.; Volak, L. P.; Houk, B. E.; Fakih, M. G.; O'Neil, B. H.; Price, T. J.; Falchook, G. S.; Desai, J.; Kuo, J.; Govindan, R.; Hong, D. S.; Ouyang, W.; Henary, H.; Arvedson, T.; Cee, V. J.; Lipford, J. R. The Clinical KRAS^{G12C} Inhibitor AMG 510 Drives Anti-Tumor Immunity. *Nature* **2019**, *575*, 217–223.

DOI: 10.1021/acs.jmedchem.9b01180
J. Med. Chem. 2020, 63, 52–65

(29) Kalgutkar, A. S.; Dalvie, D. K. Drug Discovery for a New Generation of Covalent Drugs. *Expert Opin. Drug Discovery* **2012**, *7*, 561−581.
(30) As determined by stable-isotope labelling (SILAC) experiments; see ref 28.
(31) Campuzano, I. D.; San Miguel, T.; Rowe, T.; Onea, D.; Cee, V. J.; Arvedson, T.; McCarter, J. D. High-Throughput Mass Spectrometric Analysis of Covalent Protein-Inhibitor Adducts for the Discovery of Irreversible Inhibitors: A Complete Workflow. *J. Biomol. Screening* **2016**, *21*, 136−144.
(32) Cee, V. J.; Volak, L. P.; Chen, Y.; Bartberger, M. D.; Tegley, C.; Arvedson, T.; McCarter, J.; Tasker, A. S.; Fotsch, C. Systematic Study of the Glutathione (GSH) Reactivity of *N*-Arylacrylamides: 1. Effects of Aryl Substitution. *J. Med. Chem.* **2015**, *58*, 9171−9178.
(33) Data to be reported separately.
(34) Details of this trial can be found at https://clinicaltrials.gov/ (accessed Sep 7, 2019).
(35) Fakih, M.; O'Neil, B.; Price, T. J.; Falchook, G. S.; Desai, J.; Kuo, J.; Govindan, R.; Rasmussen, E.; Morrow, P. K. H.; Ngang, J.; Henary, H. A.; Hong, D. S. Phase 1 Study Evaluating the Safety, Tolerability, Pharmacokinetics (PK), and Efficacy of AMG 510, a Novel Small Molecule KRASG12C Inhibitor, in Advanced Solid Tumors. *J. Clin. Oncol.* **2019**, *37*, 3003.

DOI: 10.1021/acs.jmedchem.9b01180
J. Med. Chem. 2020, 63, 52−65